Floating tracer clustering in divergent random flows modulated by an unsteady mesoscale ocean field

Journal:	*Geophysical & Astrophysical Fluid Dynamics*
Manuscript ID	GGAF-2020-0002.R3
Manuscript Type:	Original Article
Date Submitted by the Author:	n/a
Complete List of Authors:	Stepanov, Dmitry; V.I.Il`ichev Pacific Oceanological Institute, Ryzhov, Evgeny; V.I. Il`ichev Pacific Oceanological Institute, Berloff, Pavel; Imperial College London, Department of Mathematics Koshel, Konstantin; V.I. Il`ichev Pacific Oceanological Institute
Keywords:	Mesoscale, Submesoscale, Steady and unsteady flows, Tracer clustering, Tracer mixing
Note: The following files were submitted by the author for peer review, but cannot be converted to PDF. You must view these files (e.g. movies) online.	
GGAF-2020-0002-Koshel-General.bib GGAF-2020-0002-Koshel.tex	

Geophysical and Astrophysical Fluid Dynamics
Vol. 00, No. 00, 00 Month 0000, 1–21

Floating tracer clustering in divergent random flows modulated by an unsteady mesoscale ocean field

Dmitry V. Stepanov†, Eugene A. Ryzhov†, Pavel Berloff §, and Konstantin V. Koshel †,‡ *

†V.I.Il'ichev Pacific Oceanological Institute of FEB RAS, 43, Baltiyskaya Street, Vladivostok, 690041, Russia,
‡Institute of Applied Mathematics, FEB RAS, 7, Radio Street, Vladivostok 690022, Russia,
§Department of Mathematics, Imperial College London, London, SW7 2AZ, United Kingdom

(*0000*)

Clustering of tracers floating on the ocean surface and evolving due to combined velocity fields consisting of a deterministic mesoscale component and a kinematic random component is analysed. The random component represents the influence of submesoscale motions. A theory of exponential clustering in random velocity fields is applied to characterise the obtained clustering scenarios in both steady and unsteady time-dependent mesoscale flows, as simulated by a comprehensive realistic, eddy-resolving, general circulation model for the Japan/East Sea. The mesoscale flow field abounds in transient eddy-like patterns modulating and branching the main currents, and the underlying time-mean flow component features closed recirculation zones that can entrap the tracer. The submesoscale flow component is modelled kinematically, as a divergent random velocity field with a prescribed correlation radius and variance. The combined flow induces tracer clustering, that is, the exponential growth of tracer density in patches with vanishing areas. The statistical topography methodology, which provides integral characteristics to quantify the emerging clusters, uncovers drastic dependence of the clustering rates on whether the mesoscale flow component is taken to be steady or time-dependent. The former situation favours robust exponential clustering, similar to the theoretically understood case of purely divergent and zero-mean random velocity. The latter situation, on the contrary, hinders exponential clustering due to significant advection of the tracer out of the nearly enclosed eddies, at the rate faster than the clustering rate.

Keywords: Mesoscale; submesoscale; steady and unsteady flows; tracer clustering; tracer mixing; tracer advection

1. Introduction

Tracer transport at the ocean surface is one of the challenging problems that attract much attention due to the complexity of the dynamical processes involved in generating the transport patterns. The main difficulty in understanding these patterns comes from the multi-scale nature of the ocean currents. There are large-scale circulations (e.g., ocean gyres and currents separating them) that induce the large-scale mean advection (Pedlosky 1996, Vallis 2017). Then, the mesoscale advection is induced by mostly transient synoptic eddies (Gryanik *et al.* 2006, Chelton *et al.* 2007, McWilliams 2013, Reznik 2010, Reznik and Kizner 2010, Chelton *et al.* 2011, Sokolovskiy and Verron 2014, Koshel *et al.* 2019a), which are hard to resolve in the comprehensive general circulation models, and whose dynamics is often nonlinearly complicated and difficult to be parameterised. Further downscale there are largely unresolved submesoscale motions (Berti *et al.* 2011, Schroeder *et al.* 2012, Zhong and Bracco 2013, Berta *et al.* 2016, McWilliams 2016, Haza *et al.* 2016, Ohlmann *et al.* 2019), increasingly more researched due to the improved observational skills and spatial resolution of the circulation

* Corresponding author. Email: kvkoshel@poi.dvo.ru

models. The simplistic view on the problem assumes that these scales are well separated in the spectra and, thus, can be treated separately. We also adopt this approach, but note that often these scales are intertwined and interact via complex backscatters (Jansen and Held 2014, Jansen *et al.* 2015, Shevchenko and Berloff 2016, Bachman *et al.* 2017, Berloff 2018). All these scales contribute significantly to the floating tracer patterns and ideally should be taken into account.

Because of the many scales of motion involved, the resulting tracer patterns often exhibit spatial inhomogeneities with sharp local aggregations of tracer (Okubo 1980, McComb 1990, Law *et al.* 2010, Cozar *et al.* 2014, Martinez *et al.* 2009, Maximenko *et al.* 2012, Väli *et al.* 2018) that survive for long times. This effect is called clustering and attributed to the effect of the surface velocity divergence (Klyatskin *et al.* 1996a, Koshel and Alexandrova 1999, Klyatskin and Koshel 2000, Huntley *et al.* 2015, Jacobs *et al.* 2016, Koshel *et al.* 2019b, Stepanov *et al.* 2020) on the scales by orders of magnitude smaller than those of the dynamically dominant, coherent mesoscale eddies. The main objective of this paper is to show that the clustering process can be significantly and nontrivially altered by the interplay between the mesoscale and submesoscale velocity components.

The Eulerian evolution of the floating-tracer density, considered on the ocean surface and subject to its 2D velocity field $\boldsymbol{U}(\boldsymbol{R},t)$, is governed by the equation

$$\frac{\partial}{\partial t}\rho(\boldsymbol{R},t)+\boldsymbol{\nabla}_{\boldsymbol{R}}\left(\boldsymbol{U}(\boldsymbol{R},t)\rho(\boldsymbol{R},t)\right)=0, \qquad \rho(\boldsymbol{R},0)=\rho_0(\boldsymbol{R}), \tag{1}$$

where $\boldsymbol{R}=(x,y)$ is the horizontal position vector, $\boldsymbol{\nabla}_{\boldsymbol{R}}$ is the horizontal gradient, $\rho(\boldsymbol{R},t)$ is the tracer density distribution, $\rho_0(\boldsymbol{R})$ is the initial tracer density, and the 2D velocity field $\boldsymbol{U}(\boldsymbol{R},t)$ generally has both divergent and rotational components. We consider a combination of deterministic mesoscale and random submesoscale velocity fields

$$\boldsymbol{U}(\boldsymbol{R},t)=\underbrace{\langle\boldsymbol{U}(\boldsymbol{R},t)\rangle}_{\textbf{mesoscale}}+\underbrace{\gamma\boldsymbol{U}^p(\boldsymbol{R},t)+(1-\gamma)\boldsymbol{U}^s(\boldsymbol{R},t)}_{\textbf{submesoscale}}. \tag{2}$$

Here, superscripts s and p stand for rotational (solenoidal) and divergent (potential) random velocity components, and $\langle\dots\rangle$ is the averaging over an ensemble of random velocity field realizations. The deterministic (mesoscale) component $\langle\boldsymbol{U}(\boldsymbol{R},t)\rangle$ is given by a realistic eddy-resolving simulation of the Japan/East Sea (JES) circulation and can be treated as either steady or time-dependent. The submesoscale component is modelled by a random kinematic velocity field that comprises both divergent and rotational components, whose relative contributions are defined by parameter $0\le\gamma\le1$. The resulting clustering process is ultimately induced by the velocity divergence (Klyatskin *et al.* 1996b,a, Saichev and Woyczynski 1996, Falkovich *et al.* 2001, Eckhardt and Schumacher 2001, Schumacher and Eckhardt 2002, Cressman and Goldburg 2003, Bec *et al.* 2004, Fouxon 2012, Klyatskin 2015, Huntley *et al.* 2015, Jacobs *et al.* 2016, Klyatskin 2016, Väli *et al.* 2018). Our previous papers dealt with clustering in kinematic, zero-mean, random velocity fields (Koshel *et al.* 2019b), and also in such fields with the additional, deterministic, steady velocity component represented by realistic mesoscale flow features (Stepanov *et al.* 2020). The present work generalises and extends the previous results by considering a more complex, unsteady time-dependent mesoscale flow component and its influence on the clustering processes.

2. The mesoscale deterministic flow component model The mesoscale flow model

For the deterministic flow velocity component, we use the horizontal velocity field obtained from the realistic, primitive-equations general circulation INMOM model of the JES, which is of the sigma-coordinate type (i.e., with the vertical coordinate following the bathymetry). For

Table 1. **Parameters of the JES model**

Modelling region	$123E - 147.25E$; $28.3N - 52.1332N$
Horizontal resolution	$1/12^\circ \times 1/12^\circ$
Vertical resolution	25 sigma-levels
Sea ice model	Thermodynamic model
Unresolved scale parameterisation	2- and 4-order Laplacian along geopotential surfaces
Heat and salinity diffusivity of the second order	10 m^2/s
Heat and salinity diffusivity of the fourth order	$7 \cdot 10^9$ m^4/s
Turbulent viscosity of the second order	50 m^2/s
Turbulent viscosity of the fourth order	$7 \cdot 10^9$ m^4/s
Vertical viscosity and diffusion parameterisation	Pacanowski-Philander
Vertical diffusivity	from 10^{-6} to 0.005 m^2/s
Vertical viscosity	from 10^{-4} to 0.025 m^2/s

Table 2. **Atmospheric forcing parameters from JRA55-do dataset**

Horizontal resolution	0.5625° in the meridional and zonal directions
Time interval	1958 – 2017
Time resolution	
Meridional and zonal wind speed at height 10m	3 hours
Air temperature at height 10m	3 hours
Air humidity at height 10m	3 hours
Pressure at the sea surface	3 hours
Long- and short-wave solar radiation and rain precipitation	averaging every 3 hours
Daily-averaged river flows	included

detailed descriptions of the numerical implementations and other details (see Marchuk *et al.* 2005, Zalesny *et al.* 2017, Stepanov *et al.* 2018). Examples of the INMOM implementations include modelling of the global ocean and marginal seas (Danabasoglu *et al.* 2014, Gusev and Diansky 2014, Stepanov 2017, 2018).

For modelling the JES circulation system, several factors have to be taken into account: e.g., the atmospheric forcing and water exchange through the JES straits (Chang and Teague 2004, Chang *et al.* 2016). The water exchange is taken into account by enlarging the model domain to include the adjacent parts of the East China Sea, Okhotsk Sea and Pacific Ocean. This approach enables one to generate the unforced water inflow through the Korea/Tsushima strait in the south and the outflow through the Tsugaru and Soya straits in the east.

The lateral boundaries of the enlarged domain are no-slip for velocity, while the heat and salt fluxes are equal to zero. Near the open boundaries, we implemented the relaxation layers with spatial extent $\sim 1^\circ$, where the potential temperature and salinity profiles are nudged to their climatological monthly means (taken from the WOA2013 v2.0 dataset: Locarnini *et al.* 2013, Zweng *et al.* 2013).

The model has horizontal resolution of $1/12^\circ$ in both zonal and meridional directions. Since the first baroclinic Rossby radius of deformation is 10–15km in the southern part of the domain (to the south of 41°N) and 5–10km in the northern part, the spatial resolution varies from eddy-resolving in the south to eddy-permitting in the north. The sigma-coordinate levels, which characterise the vertical resolution, are finer near the surface and bottom, thus, enabling a better resolution of the surface and bottom boundary layers.

The second- and fourth-order Laplacians are used to account for the horizontal turbulent viscosity and diffusivity, respectively; the vertical turbulent viscosity and diffusivity are factored in through the Pacanowski-Philander parameterisation (Pacanowski and Philander 1981). Table 1 lists the implemented parameter values.

The surface atmospheric forcing, represented by a combination of heat, fresh-water, and momentum fluxes, is given by the bulk relations (Large and Yeager 2009). The atmospheric parameters are taken from the JRA55-do dataset (Tsujino *et al.* 2018), as presented in Table 2.

The temperature conditions in the JES favour ice formation in its northern part — this significantly alters the temperature and fresh-water balances at the surface and, thus, may

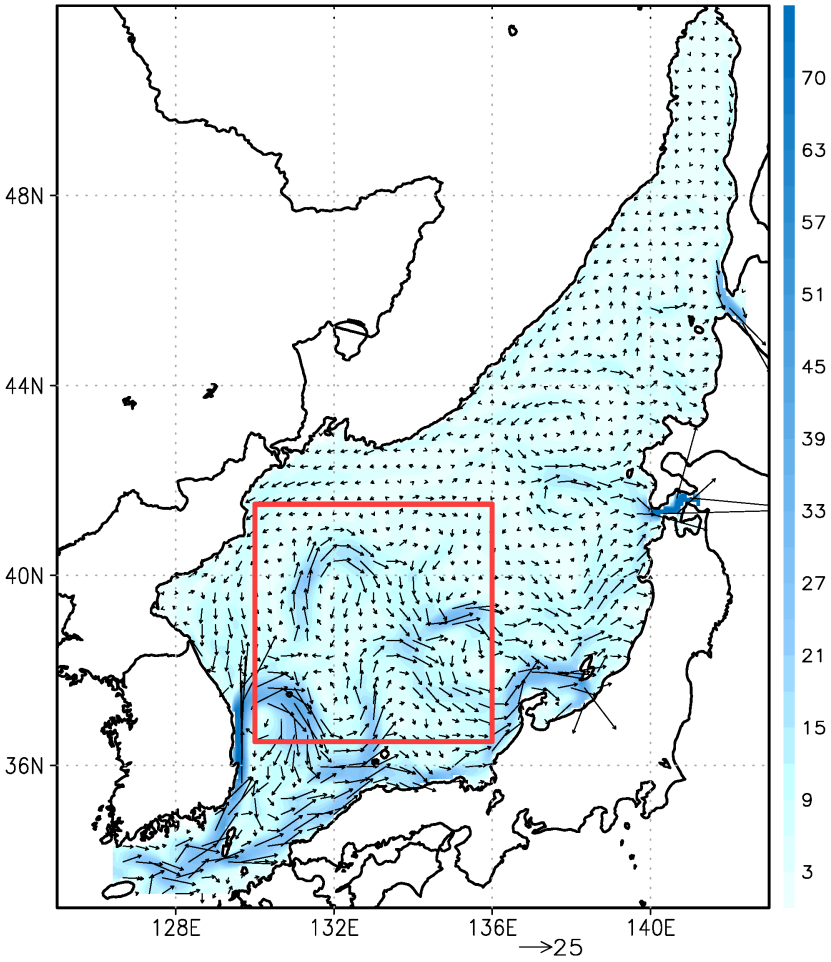

Figure 1. Multi-year mean (from 1980 to 2008) surface velocity field of the JES (shading, cm s^{-1}) from the eddy-resolving model. (Colour online).

influence the Primorye current. Hence, for a better representation of the JES circulation, we also exploit the thermodynamic and dynamic ice cores of the INMOM (Yakovlev 2009).

For the initial conditions, we use potential temperature and salinity fields from the WOA2013v2.0 dataset (spatial resolution 1/4° with 102 standard depth levels). Various factors, such as the model configuration's overall simplicity, inaccuracies of parameterisations and boundary conditions, contributed towards accumulated simulation errors, as compared to the observed mean values. To ameliorate the errors, we nudge potential temperature and salinity in the 50-meter mixed layer to their climatological values, with the nudging coefficients of 1 month for potential temperature and 3 months for salinity.

The model is run from 1958 to 2017. After 10 years, the kinetic energy and temperature, averaged over the JES at various depth layers, become nearly stationary. For the tracer transport and our clustering analysis, we used the velocity field on the sea surface from 01 March to 30 April 2000.

The spatial pattern of the multi-year mean surface circulation (figure 1) features the pronounced Tsushima Warm Current (TWC) (Chang *et al.* 2016), flowing through the Korea/Tsushima Strait to the JES. Its shore branch (the Neashore branch of the TWC) flows through the strait's eastern part and extends along the eastern part of the JES. The current outflows partially through the Tsugaru Strait, another part branches near 44N to the north-western part of the JES, while the rest of the current follows to the north and exits through the Soya Strait. The western branch of the TCW inflows through the strait's western part, and then splits into the East Korea Warm Current (EKWC) and Offshore Branch of the TWC. The EKWC generates a mesoscale anticyclonic eddy.

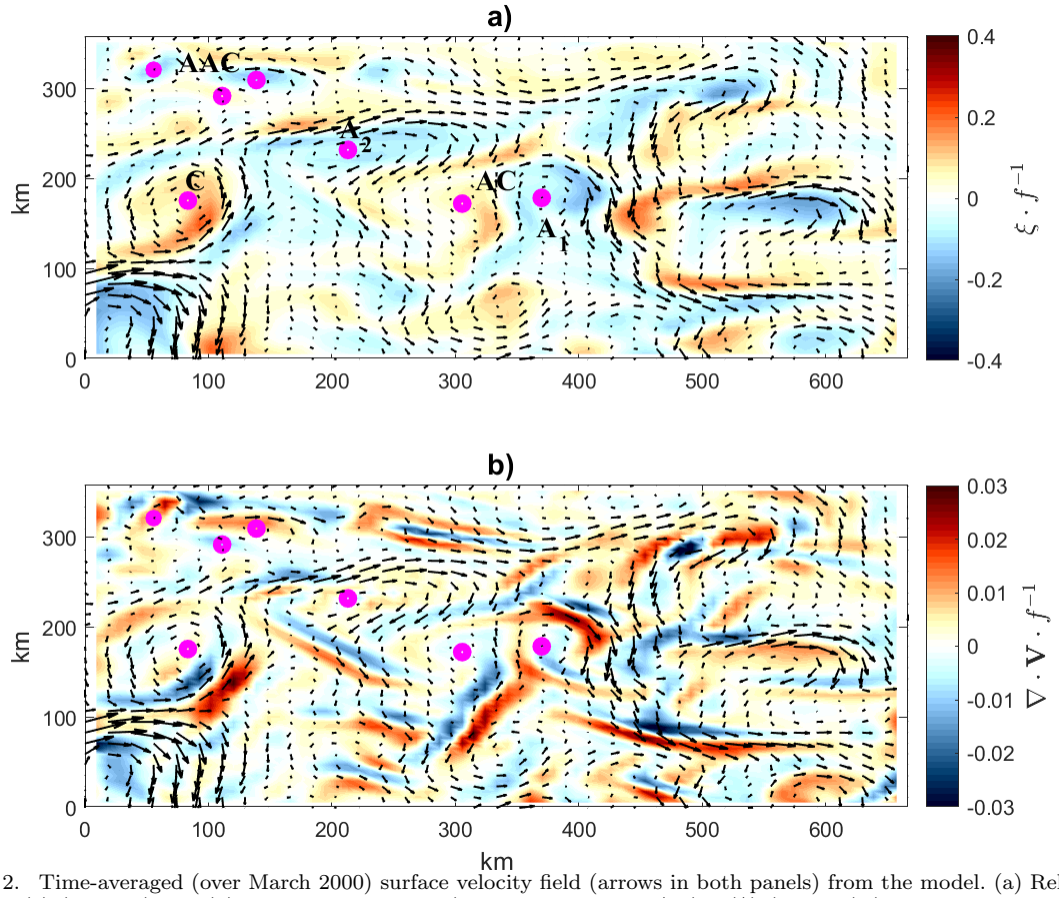

Figure 2. Time-averaged (over March 2000) surface velocity field (arrows in both panels) from the model. (a) Relative vorticity (ξ) (shading) and (b) velocity divergence ($\boldsymbol{\nabla_R}\cdot\boldsymbol{V}$, where $\boldsymbol{V} = \langle \boldsymbol{U}(\boldsymbol{R},t)\rangle$) (shading) (both normalised by the Coriolis parameter f). Tracer deployment sites are marked by letters (see explanation in the text). Purple points denote the centres of the mesoscale eddies. (Colour online).

2.1. *Characteristics of the deterministic velocity component*

For further analysis of the tracer evolution and clustering in combined deterministic/random velocity field, we chose a subdomain of JES, which is indicated by a red square in figure 1. The subdomain is characterised by strong mesoscale activity throughout the year, thus, demonstrating highly nonstationary flow patterns, which induce complex tracer transport. Since one of our goals is to compare tracer clustering scenarios for stationary and nonstationary deterministic velocity components, first, we assess the characteristics of the averaged over March 2000 velocity field: in figure 2 arrows represent the velocity field, and colour-coded are both relative vorticity (figure 2(a)) normalised by the Coriolis parameter, f, and 2D velocity divergence $\boldsymbol{\nabla_R}\cdot\langle \boldsymbol{U}(\boldsymbol{R},t)\rangle$ (figure 2(b)).

The averaged velocity field features many cyclonic and anticyclonic coherent eddy-like structures (see the relative vorticity in figure 2(a)) with strong horizontal shears. Characteristic length scale of the eddies ($\sim$ 40 km), which is 2-2.5 times the local first baroclinic Rossby radius, allows us to categorise these structures as mesoscale ones. The 2D surface velocity attests that the eddies are associated with zones of significant surface divergence (convergence).

The divergence (figure 2(b)) reaches its extreme values mostly along the jets and at periphery of the eddies. At the periphery of cyclonic eddies $\boldsymbol{\nabla_R}\cdot\langle \boldsymbol{U}(\boldsymbol{R},t)\rangle < 0$ (cyclone C), while for the anticyclone peripheries this is on the opposite $\boldsymbol{\nabla_R}\cdot\langle \boldsymbol{U}(\boldsymbol{R},t)\rangle > 0$ (anticyclone A1). At the centres of cyclones/anticyclones, the absolute value of divergence is noticeably smaller, and the divergence is predominantly positive/negative.

Since the velocity field is nonstationary (taken with the hourly data and interpolated in time), both divergence and vorticity significantly deviate from their means. We consider full time dependence of the mesoscale field from 01 March to 30 April of 2000. Instantaneous snapshots of the velocity field with the overlayed vorticity, normalised by f (figure 3) illustrate that the currents have weakened during this time interval. Certain eddy structures (anticyclone A2 and smaller eddies AAC) are absent from the instantaneous field but present in the mean field. Cyclone C and anticyclone A1, on the other hand, persist but are significantly deformed.

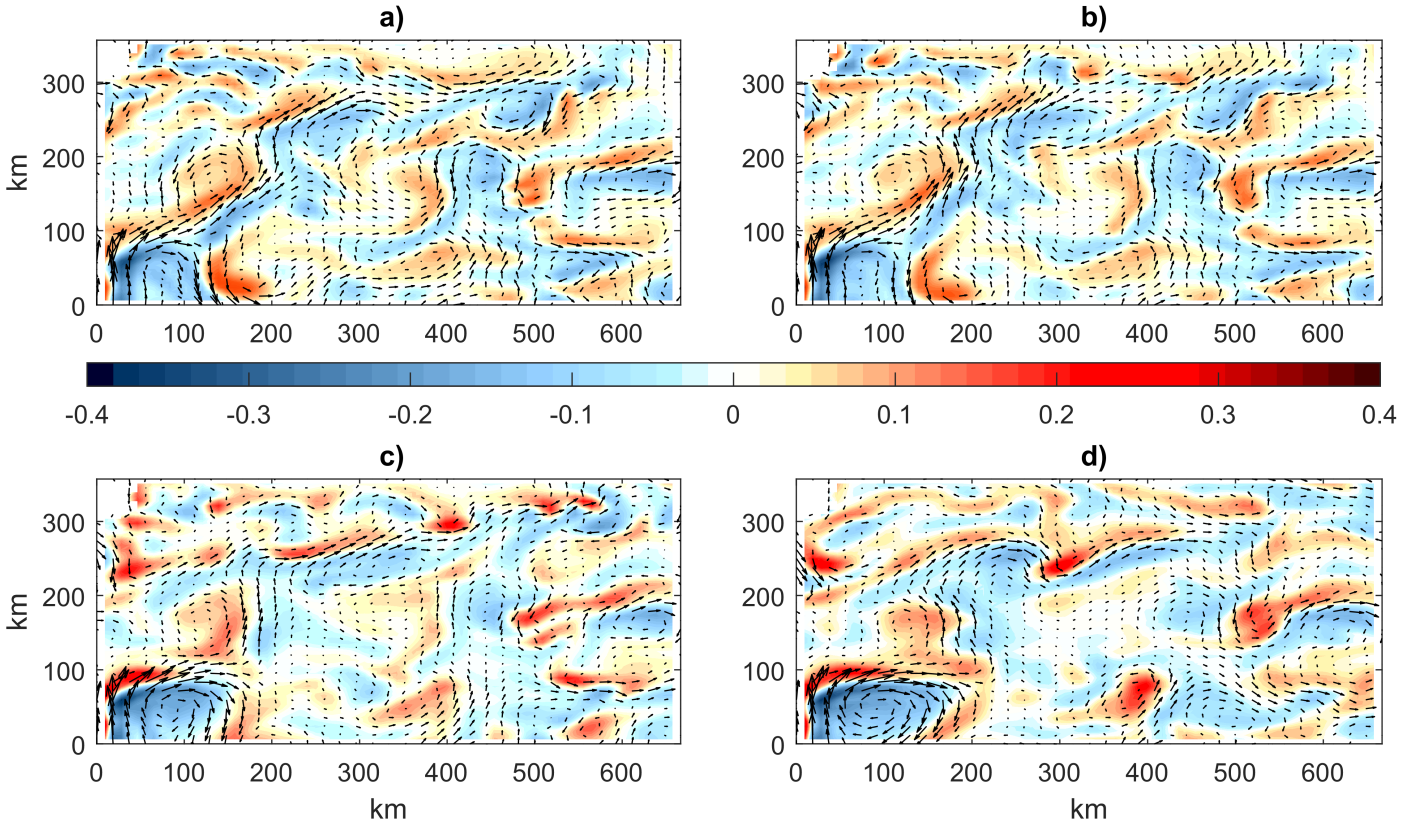

Figure 3. Instantaneous velocity snapshots overlayed with vorticity (ξ) normalised by the Coriolis parameter f (colour-coded) at depth level 50 m in year 2000: a) 1 March, b) 5 March, c) 20 March and d) 8 April. (Colour online).

The corresponding divergence field (figure 4), also normalised by f, is significantly spatially inhomogeneous. The largest gradients of the divergence are observed near the regions, where eddies interact with the large-scale flow. Particularly, we observe that during several days divergence at the periphery of cyclone C alters its sign; after that the jet weakens, and the absolute value of divergence decreases. Another example shows how divergence at the anticyclone A2 centre noticeably subsides in only a few days. These big changes in the divergence and vorticity fields influence tracer advection and clustering rates and will be addressed further.

3. Random velocity field as a model for submesoscale motions

The submesoscale component is assumed to be represented by a random velocity field, which is statistically homogeneous in space and stationary in time, and consists of solenoidal (non-divergent) and potential (divergent) components. We also assume that these components have Gaussian PDFs, and are statistically isotropic in space and δ-correlated in time. Then, the space-time correlation tensor (Klyatskin 1994, 2015) for spatial shift R' and time lag η is

$$B^j_{\alpha\beta}(\boldsymbol{R'},\eta) = \langle U^j_\alpha(\boldsymbol{R},t)U^j_\beta(\boldsymbol{R}+\boldsymbol{R'},t+\eta)\rangle = \int \mathrm{d}\boldsymbol{k}\, E^j_{\alpha\beta}(\boldsymbol{k},\eta)\mathrm{e}^{\mathrm{i}\boldsymbol{k}\cdot\boldsymbol{R'}}\,, \qquad (3)$$

where indices α and β represent x and y, index j stands for p (potential) and s (solenoidal), and indicates different tensors; $\boldsymbol{k} = (k_x, k_y)$ is the 2D wavevector, $k = |\boldsymbol{k}|$.

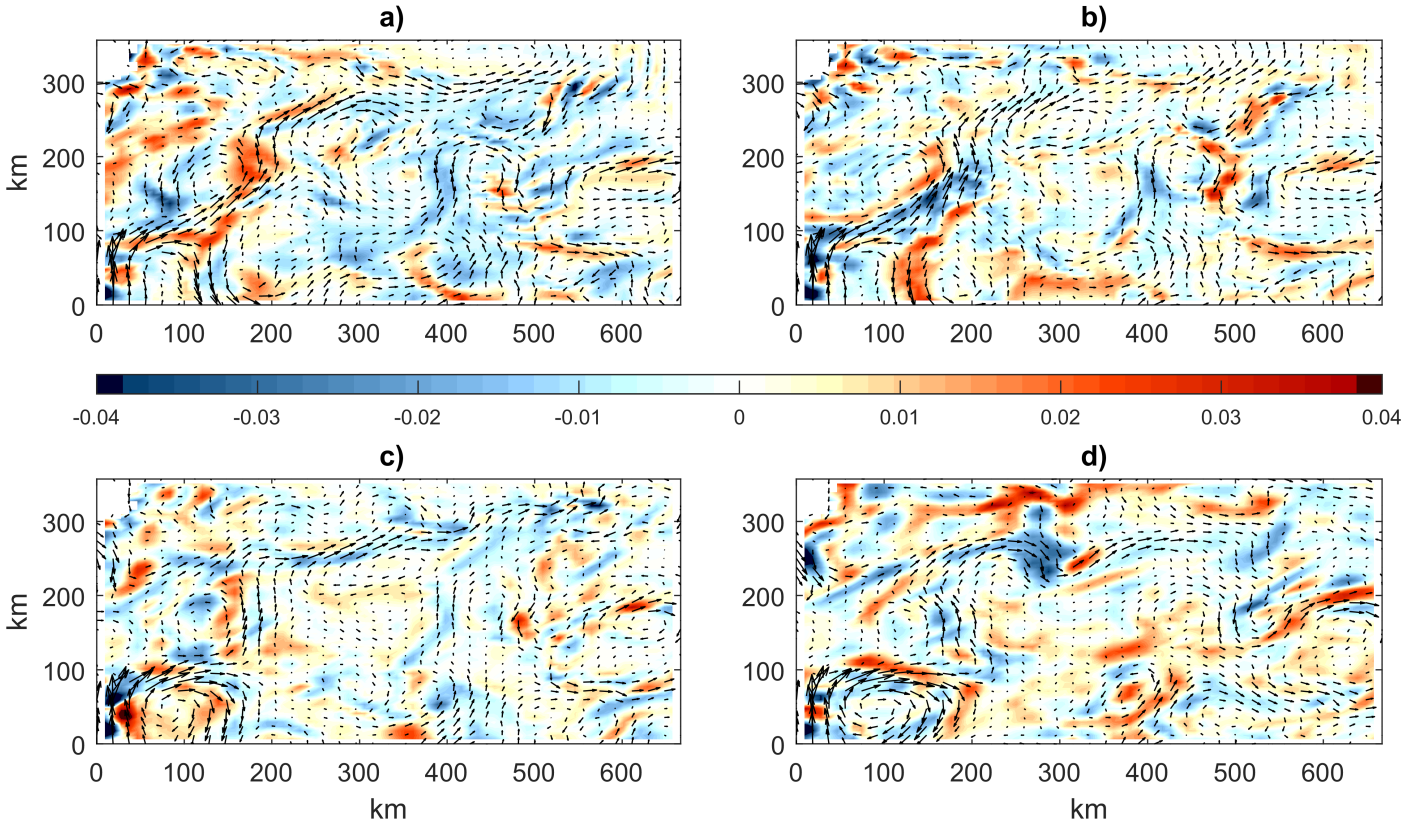

Figure 4. The same as in figure 3, but with colour-coded divergence $\boldsymbol{\nabla}_{\boldsymbol{R}}\cdot\langle\boldsymbol{U}(\boldsymbol{R},t)\rangle$ normalised by the Coriolis parameter (f). (Colour online).

The following spectral densities are implemented

$$E^{p}_{\alpha\beta}(\boldsymbol{k},\eta)=E^{p}(k,\eta)\frac{k_\alpha k_\beta}{k^2}\,,\qquad E^{s}_{\alpha\beta}(\boldsymbol{k},\eta)=E^{s}(k,\eta)\left(\delta_{\alpha\beta}-\frac{k_\alpha k_\beta}{k^2}\right)\,, \tag{4}$$

where $\delta_{\alpha\beta}$ is the Kroeneker delta. Single-point correlations define the velocity variance σ_U^2, such that

$$\sigma_U^2=B_{\alpha\alpha}(\boldsymbol{0},0)=\int \mathrm{d}\boldsymbol{k}\,E(k,0), \tag{5a}$$

$$B^{j}_{\alpha\beta}(\boldsymbol{0},0)=\langle U^{j}_{\alpha}(\boldsymbol{R},t)U^{j}_{\beta}(\boldsymbol{R},t)\rangle=\tfrac{1}{2}\sigma_U^2\delta_{\alpha\beta}\,. \tag{5b}$$

3.1. *Numerical implementation of the random velocity field*

A spectral representation of the velocity field (Roberts and Teubner 1995, Zirbel and Cinlar 1997, Koshel and Alexandrova 1999, Klyatskin and Koshel 2017) is given by

$$U^{p}_{\beta}(\boldsymbol{R},t)=\sigma_{\boldsymbol{U}}\int \mathrm{d}\boldsymbol{k}\big(a(k,t)+\mathrm{i}b(k,t)\big)\frac{k_\beta}{k}\exp(\mathrm{i}\boldsymbol{k}\cdot\boldsymbol{R}), \tag{6a}$$

$$U^{s}_{x}(\boldsymbol{R},t)=\sigma_{\boldsymbol{U}}\int \mathrm{d}\boldsymbol{k}\big(a(k,t)+\mathrm{i}b(k,t)\big)\frac{k_y}{k}\exp(\mathrm{i}\boldsymbol{k}\cdot\boldsymbol{R}), \tag{6b}$$

$$U^{s}_{y}(\boldsymbol{R},t)=-\sigma_{\boldsymbol{U}}\int \mathrm{d}\boldsymbol{k}\big(a(k,t)+\mathrm{i}b(k,t)\big)\frac{k_x}{k}\exp(\mathrm{i}\boldsymbol{k}\cdot\boldsymbol{R}), \tag{6c}$$

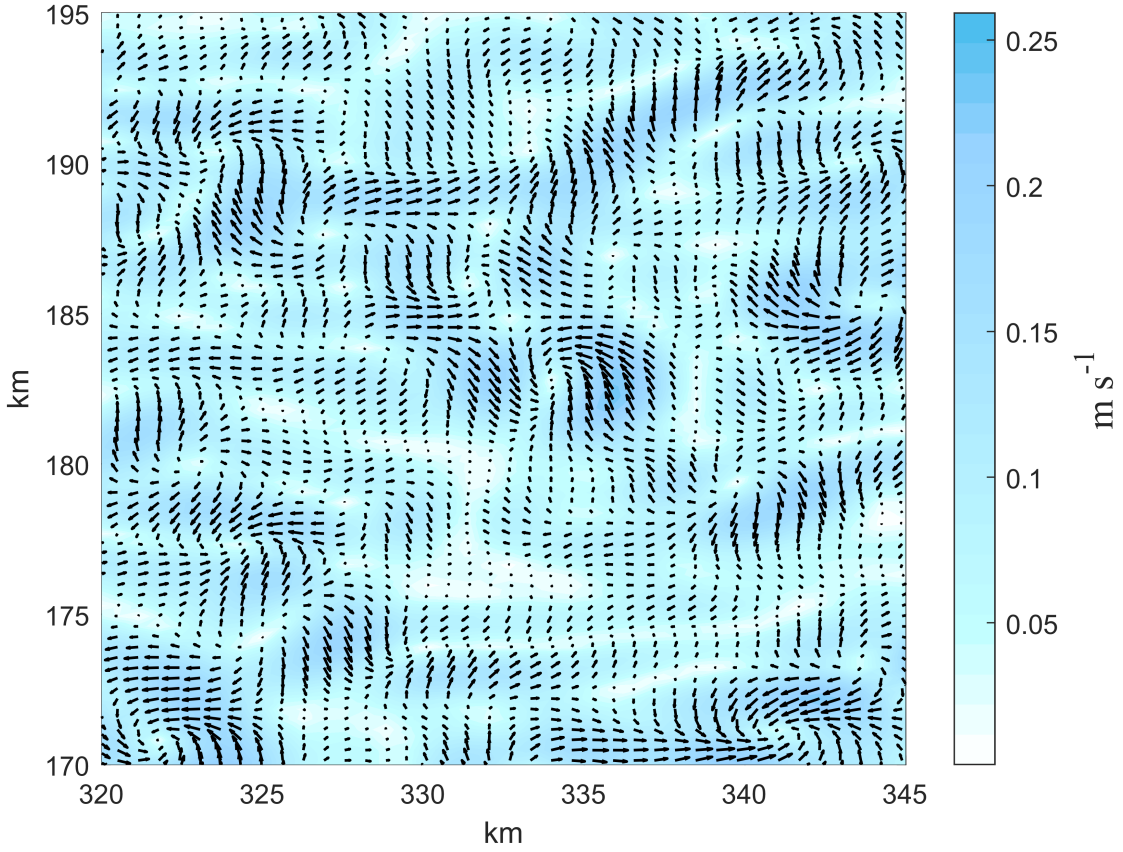

Figure 5. A realisation of the random velocity field; shown on a smaller subdomain, for parameters $\sigma_U = 0.1$, $l = 0.08$, and $\gamma = 0.5$. Colour-coded is the length of the random velocity vector. (Colour online).

where σ_U controls the intensity; index β stands for either x or y; $a(\boldsymbol{k},t)$ and $b(\boldsymbol{k},t)$ are Gaussian, random, δ-correlated in time, spectral coefficients to satisfy

$$\langle a(k,t)\rangle = \langle b(k,t)\rangle = \left\langle a(\boldsymbol{k},t)b(\boldsymbol{k'},t')\right\rangle = 0, \tag{7a}$$

$$\left\langle a(\boldsymbol{k},t)a(\boldsymbol{k'},t')\right\rangle = \left\langle b(\boldsymbol{k},t)b(\boldsymbol{k'},t')\right\rangle = E(k)\delta(\boldsymbol{k}-\boldsymbol{k'})\delta(t-t')\,. \tag{7b}$$

The inverse Fourier transform of a realisation yields random velocity field with the correlation tensor (3). The implemented spectral density with a prescribed correlation radius l is

$$E(k;l) = \frac{1}{2\pi}\,\frac{l^4}{4}\,k^2\,\exp\left(-\frac{1}{2}\,k^2\,l^2\right)\,. \tag{8}$$

In the physical space, the random velocity field is generated on the uniform grid 2048×2048. figure 5 illustrates one random velocity realisation with equal relative contributions of the potential and rotational components ($\gamma = 0.5$).

3.2. *Lagrangian approach for solving the advection equation*

The governing equation (1) is solved using the Lagrangian representation

$$\frac{\mathrm{d}\boldsymbol{R}(t)}{\mathrm{d}t} = \boldsymbol{U}(\boldsymbol{R}(t),t), \qquad \boldsymbol{R}(0) = \boldsymbol{\xi}, \tag{9a}$$

$$\frac{\mathrm{d}\rho}{\mathrm{d}t} = \boldsymbol{\nabla}_{\boldsymbol{R}}\cdot\boldsymbol{U}(\boldsymbol{R}(t),t)\rho(t), \qquad \rho(0) = \rho_0(\boldsymbol{\xi})\,. \tag{9b}$$

The tracer initial distribution is given by a set of particles with positions $\boldsymbol{\xi}_i$, $(1 \le i \le N)$. The tracer patch size is chosen to encompass eddies in the deterministic flow. Each particle trajectory, together with particle tracer density, is followed by solving the system of characteristic equations (9) as a set of stochastic ODEs, by using the standard Euler-Îto scheme (Kloeden and Platen 1992, Koshel and Alexandrova 1999). The Eulerian density can be approximated by coarse graining over the particles.

3.3. *Statistical topography of random fields*

To analyse clustering properties of the numerical solutions, we resort to the statistical topography methodology (Isichenko 1992, Klyatskin 2003) and find the key integral characteristics. The method involves calculating effective diffusion coefficients for the potential (D^p) and solenoidal (D^s) velocity components:

$$\begin{aligned} D^p &= \int_0^\infty \mathrm{d}\eta \int \mathrm{d}\boldsymbol{k}\, k^2 E^p(k,\eta) \\ &= \int_0^\infty \mathrm{d}\eta \left\langle \left(\boldsymbol{\nabla}_{\boldsymbol{R}}\cdot\boldsymbol{U}(\boldsymbol{R},t+\eta)\right)\left(\boldsymbol{\nabla}_{\boldsymbol{R}}\cdot\boldsymbol{U}(\boldsymbol{R},t)\right)\right\rangle = \gamma^2 D^0\,, \end{aligned} \tag{10a}$$

$$\begin{aligned} D^s &= \int_0^\infty \mathrm{d}\eta \int \mathrm{d}\boldsymbol{k} k^2 E^s(k,\eta) \\ &= \frac{1}{2}\int_0^\infty \mathrm{d}\eta \left\langle \left(\boldsymbol{\nabla}\times\boldsymbol{U}(\boldsymbol{R},t+\eta)\right)\cdot\left(\boldsymbol{\nabla}\times\boldsymbol{U}(\boldsymbol{R},t)\right)\right\rangle = (1-\gamma)^2\, D^0\,, \end{aligned} \tag{10b}$$

$$D^0 = \frac{\sigma_U^2}{l^2} t_0\,, \tag{10c}$$

where D^0 depends on the free parameters σ_U and l, and on the dimensional time scale t_0 chosen to be equal to the numerical discretisation time step. The diffusion coefficients are associated with the effective correlation tensor and its second derivatives

$$B_{kl}^{eff}(\boldsymbol{r}) = \int_0^\infty \mathrm{d}\tau\, B_{kl}(\boldsymbol{r},\tau), \qquad B_{kl}^{eff}(0) = D^0\delta_{kl}, \qquad \frac{\partial}{\partial r_i} B_{kl}^{eff}(0) = 0, \tag{11a}$$

$$-8\frac{\partial^2}{\partial r_i \partial r_j} B_{kl}^{eff}(0) = D^s\left(2\delta_{kl}\delta_{ij} - \delta_{ki}\delta_{lj} - \delta_{kj}\delta_{li}\right) + D^p\left(2\delta_{kl}\delta_{ij} + \delta_{ki}\delta_{lj} + \delta_{kj}\delta_{li}\right). \tag{11b}$$

Statistical topography characteristics are defined through the indicator function

$$\varphi(\boldsymbol{R},t;\rho') = \delta(\rho(\boldsymbol{R},t) - \rho')\,, \tag{12}$$

which filters out values of the density $\rho(\boldsymbol{R},t)$ different from a prescribed value ρ', by using the Dirac δ-function. The total area of the regions, where ρ exceeds some threshold $\bar{\rho}$, is referred to as the cluster area. The total mass of the floating tracer within the cluster area is referred to as the cluster mass. Then, the area occupied by the clustered tracer and the corresponding

mass are found as

$$S(t;\bar{\rho}) = \int \mathrm{d}\boldsymbol{R}\,\theta\big(\rho(\boldsymbol{R},t)-\bar{\rho}\big) = \int \mathrm{d}\boldsymbol{R}\int_{\bar{\rho}}^{\infty}\mathrm{d}\rho'\,\varphi(\boldsymbol{R},t;\rho'), \tag{13a}$$

$$M(t;\bar{\rho}) = \int \mathrm{d}\boldsymbol{R}\,\rho(\boldsymbol{R},t)\,\theta\big(\rho(\boldsymbol{R},t)-\bar{\rho}\big) = \int \mathrm{d}\boldsymbol{R}\int_{\bar{\rho}}^{\infty}\mathrm{d}\rho'\,\rho'\,\varphi(\boldsymbol{R},t;\rho')\,, \tag{13b}$$

where $\theta(\cdot)$ is the Heaviside (step) function and $\bar{\rho}$ is a given density threshold value.

The exponential clustering of tracer with the net mass M_0 is, then, defined as both limits

$$\lim_{t\to\infty} S(t;\bar{\rho}) \;\to 0\,, \tag{14a}$$

$$\lim_{t\to\infty} M(t;\bar{\rho}) \;\to M_0 \tag{14b}$$

are simultaneously satisfied for any threshold $\bar{\rho}$.

It is instrumental to write down established asymptotics for the purely divergent case, when the limits are satisfied, signifying that tracer clustering occurs with probability one (Klyatskin 1994, 2015). Ensemble averaging over many realizations of the random velocity field yields

$$\langle S(t;\bar{\rho})\rangle = \int \mathrm{d}\boldsymbol{R}\int_{\bar{\rho}}^{\infty}\mathrm{d}\rho'\,P(\boldsymbol{R},t;\rho')\,, \tag{15a}$$

$$\langle M(t;\bar{\rho})\rangle = \int \mathrm{d}\boldsymbol{R}\int_{\bar{\rho}}^{\infty}\mathrm{d}\rho'\,\rho'\,P(\boldsymbol{R},t;\rho')\,, \tag{15b}$$

written through the one-point PDF

$$P(\boldsymbol{R},t;\rho) = \big\langle \delta\big(\rho(\boldsymbol{R},t)-\rho\big)\big\rangle. \tag{16}$$

Following Klyatskin (1994, 2015), one can write down expressions for the ensemble-averaged cluster area and mass

$$\begin{aligned}\langle s_{hom}(t,\bar{\rho})\rangle &= \Pr\left(\frac{\ln(\rho_0\,\mathrm{e}^{-D^p t}/\bar{\rho})}{\sqrt{2D^p t}}\right)\\ &= P\{\rho\,(\boldsymbol{R},t)>\bar{\rho}\} \approx \sqrt{\frac{\rho_0}{\pi\bar{\rho}D^p t}}\exp\big(-\tfrac{1}{4}D^p t\big),\end{aligned} \tag{17a}$$

$$\langle m_{hom}(t,\bar{\rho})\rangle = \Pr\left(\frac{\ln(\rho_0\,\mathrm{e}^{D^p t}/\bar{\rho})}{\sqrt{2D^p t}}\right), \tag{17b}$$

$$\frac{\langle m_{hom}(t,\bar{\rho})\rangle}{\rho_0} \approx 1-\sqrt{\frac{\rho_0}{\pi\bar{\rho}D^p t}}\exp\big(-\tfrac{1}{4}D^p t\big)\,, \tag{17c}$$

where ρ_0 is the initial density, which we choose equal to 1. These estimates frame the maximal rates of clustering achieved in purely divergent flows; they will be used to benchmark the other solutions. It is convenient to define the diffusion time

$$\tau = D^p t = t/\tau_p, \qquad\qquad \tau_p = 1/D^p, \tag{18}$$

with the diffusion time scale τ_p.

In the numerical simulations we define the cluster mass to be proportional to the number of particles with the density exceeding the given threshold, whereas the cluster area is the sum of all the areas of these particles, each of which is defined as $m^p/\rho_i^p\,(t)$, where m^p is the constant mass of a particle (prescribed and the same for each particle) and $\rho_i^p\,(t)$ is the density of i-th particle. The Eulerian tracer density is obtained by averaging information on the particles over the grid cell. All the integral characteristics are calculated without averaging. Moreover, since computing trajectories for millions of particles is expensive, the tracer evolution is assessed only in subdomain designated in figure 1 and containing qualitatively different flow regimes.

4. Clustering constrained by the mesoscale velocity field

Our main goal is to analyse the tracer evolution and clustering rates, when constrained by nonstationary deterministic velocity fields. For the stationary and nonstationary cases of the deterministic mesoscale field, we formulated the following 4 experiments aiming to clarify the range of possible behaviours:

(i) EXP1 — only the mesoscale field without a submesoscale (random) one;
(ii) EXP2 — plus the purely solenoidal random velocity field ($\gamma = 0$);
(iii) EXP3 — plus the purely divergent random velocity field ($\gamma = 1$);
(iv) EXP4 — plus the mixed random velocity field ($\gamma = 0.5$).

The numerical implementation involves interpolating the deterministic velocity component onto 2048×2048 grid, where the random velocity field is defined. The dimensional units are the grid size 250 m, time step 84 s, submesoscale (random) velocity scale 3 m s^{-1} with its dimensionless standard deviation $\sigma_U = 0.1$ and correlation radius $l = 2$km, all chosen so that the Rossby number is close to one. The time intervals with the saved deterministic velocity data are one hour (with linear interpolation in between).

Before plotting the density distributions, we first average them as follows. In each grid cell, an averaged density is plotted, i.e. the net mass of all Lagrangian particles located in the cell $m(i, j)$ divided by the area taken by the particles. The area is proportional to $\sum_{q=1}^{n} 1/\rho_q$, where n is the number of particles in the cell, ρ_q is the Lagrangian density of a particle accumulated along its trajectory.

4.1. *Stationary mesoscale field*

To establish reference solutions, we first consider a stationary deterministic velocity field (Stepanov *et al.* 2020) with the time averaging over March 2000. The initial tracer distribution (dimensionless time $t = 0$) is marked by a grey square in the following figures; and their upper panels correspond to $\sim$20 days, the bottom ones correspond to ($\sim$40 days).

When velocity field consists only of the deterministic component (EXP1), the tracer is simply advected around. The tracer distribution initially remains qualitatively the same (figure 6). If the tracer is initially enclosed inside an eddy (cyclone C and anticyclone/cyclone pair AC in figure 2), it remains there permanently since the eddy is stationary and tracer trajectories move along constant pressure levels; and the tracer initialised outside the eddy regions is advected out of the domain.

Adding the purely rotational ($\gamma = 0$ in (2)) submesoscale component insignificantly changes the tracer pattern (figure 7) and slightly erodes tracer boundaries, in a way similar to the effect of diffusion (Koshel *et al.* 2013, 2015). Exponential clustering, as the theory predicts, does not occur. The largest density values do not exceed $\rho_{max}/\rho_0 \sim 30$ (in the averaging sense over the velocity grid cell; without averaging the value does not change from the initial one), and they remain bounded for the integration time.

The clustering does occur when the submesoscale component is purely divergent ($\gamma = 1$), i.e., in EXP3 (figure 8), and the tracer is clustered in narrow stripes with high density values. Maximal density values observed are of the order $\rho_{max}/\rho_0 \sim 10^{12} - 10^{14}$ at time $\sim$20 days, and they are as large as $\rho_{max}/\rho_0 \sim 10^{18} - 10^{21}$ for $\sim$40 days. These anomalous values attest to the exponential nature of clustering.

Clustering also manifests itself with mixed submesoscale component ($\gamma = 0.5$), i.e., in EXP4 (figure 9), but the clustering rates and maximum density values are orders of magnitude smaller than in EXP3. Maximum density values are $10^5 - 10^6$ for $\sim$20 days and $10^8 - 10^9$ for $\sim$40 days.

To present further evidence of the exponential nature of clustering, we explore statistical

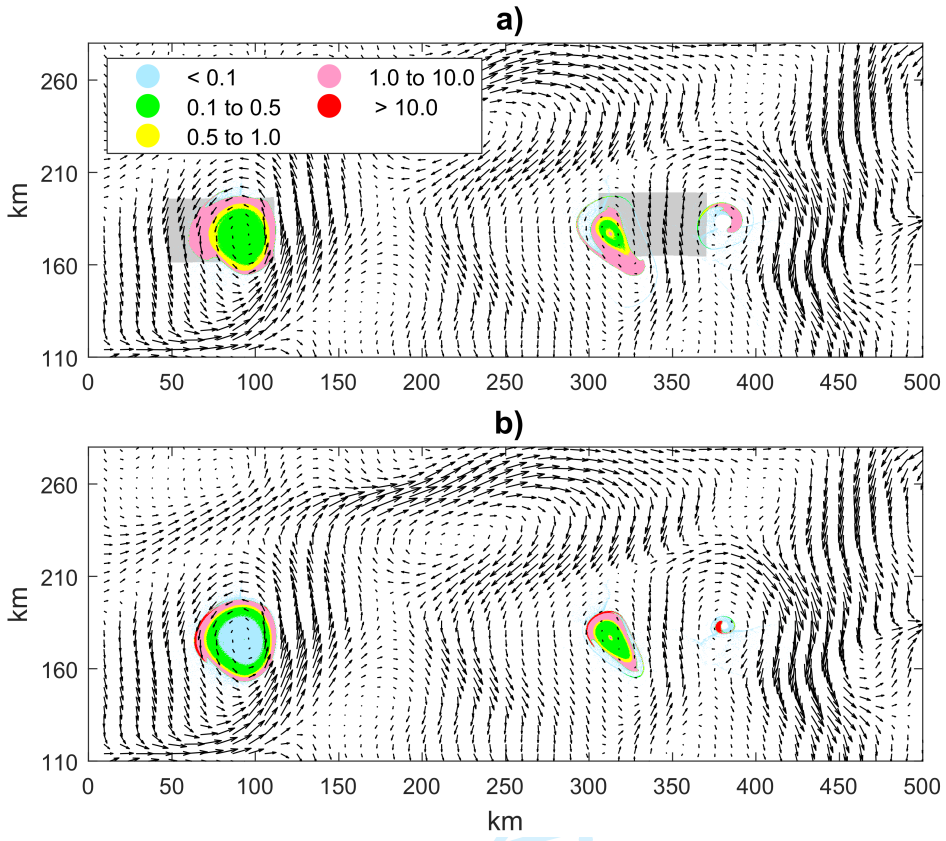

Figure 6. Tracer density evolution of cyclone C and pair AC in EXP1 after: a) 20 days and b) 40 days. (Colour online).

topography characteristics: clustering area (s) and mass (m). In the exponential clustering process, the clustering area tends to zero, whilst the clustering mass tends to the net tracer mass. All the tracer is clustered in the infinite time limit, but only finite times are at our disposal in the numerical simulations.

The clustering rates for the divergent and mixed submesoscale velocity cases exhibit clear exponential tendencies (the top curves in figure 10(a) indicate the accumulated clustering mass, the bottom curves indicate the clustering area; compare to the thick top black line that shows the asymptotic tendency (17) for the purely divergent case without deterministic component). Despite the fact that the purely divergent case (EXP3) yields much larger density values, in comparison with the mixed case (EXP4), the statistical topography characteristics demonstrate similar clustering behaviours in both cases (solid curves – EXP3; dashed curves — EXP4 in figure 10(a,b)). Moreover, clustering rates remain largely the same for different tracer deployment sites (blue curves correspond to the cyclonic eddy C; red curves correspond to the anticyclone/cyclone pair AC).

Logarithmic-scale curves (figure 10(b)) illustrate impact of the mesoscale field. It is weak on short time scale ($\sim \tau_p$) and results in reduced clustering rates, which correspond to the asymptotic diffusion coefficient $0.75D_p$. Clustering mass curves (figure 10(c)) also demonstrate reduced clustering rate on short time scales ($\tau \sim 4-8$). For EXP3 the long-term mass accumulation rate is slower compared to the corresponding clustering area shrinkage rate but still exhibits exponential tendencies. For EXP4 the mass accumulation is either drastically hindered or stopped altogether at levels of total mass accumulation close to 1 (0.85-0.95). For both EXP3 and EXP4, in terms of the non-normalised time (figure 10(d)), the clustering rate is proportional to γ^2, and the area is clustered at a reduced rate (by 75%).

As expected from the theory, the clustering rates are controlled by the divergent veloc-

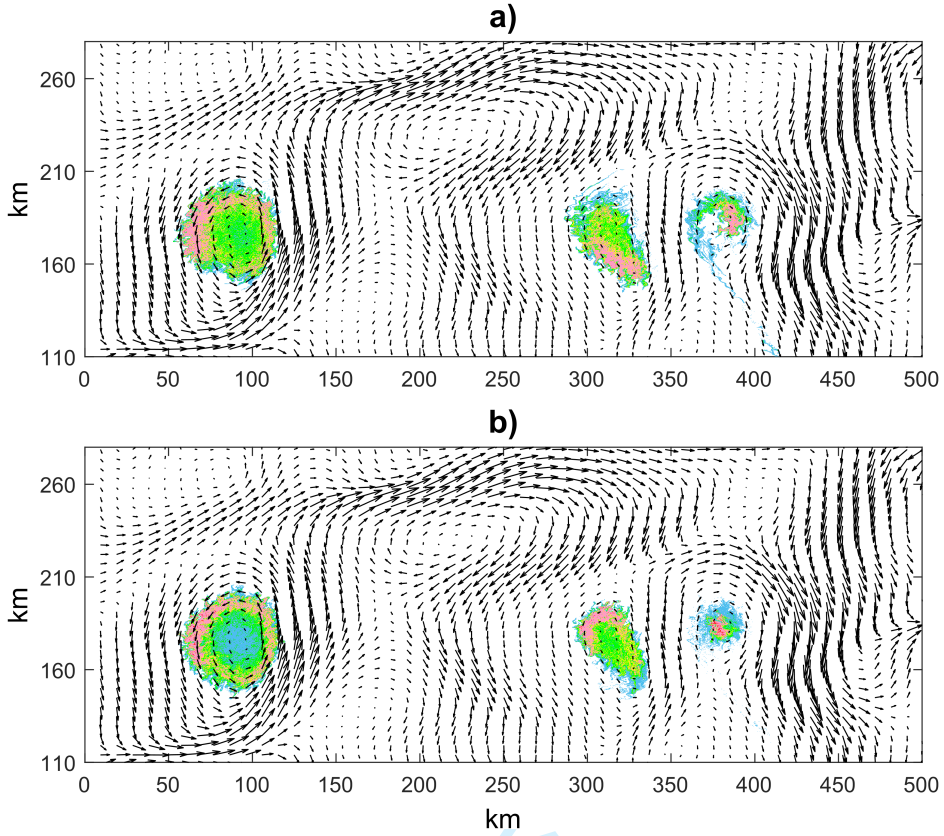

Figure 7. The same as in figure 6, but for EXP2. Advected patterns remain mostly unchanged, whilst the tracer boundaries are eroded. (Colour online).

ity component, nevertheless, the fact, that the mixed velocity case still exhibits clustering, although at slower rates (of order γ^2, see 10(d)), is worth attention and account.

5. Clustering constrained by the nonstationary mesoscale field

Since the mesoscale eddy fields are non-stationary (McWilliams 1984, Chelton *et al.* 2007, 2011, Barbosa Aguiar *et al.* 2013, Samelson 2013, Abernathey and Haller 2018), it is important to understand sensitivity of clustering to the unsteadiness. The clustering can be significantly hindered because the characteristic time scales for tracer aggregation can be constrained by the mesoscale variability time scales. Here, we do not attempt to analyse in detail the relation between these time scales and only point out the general possibility of the above scenario.

Now, instead of considering the average mesoscale velocity field, we make use of interpolated hourly outputs of the mesoscale model and consider the same experiments EXP1–EXP4, but now with the time-dependent deterministic flow. Two tracer deployment sites correspond to the anticyclonic and cyclonic eddies (marked in figure 2 as A2 and C, respectively).

When only the mesoscale velocity acts on tracer, the advection patterns for both deployment sites (see figure 11 for the cyclone and figure 12 for the anticyclone) feature typical spiral-like patterns characteristic of mesoscale-induced advection often observed by satellites and drifters. In this case (EXP1), the density remains largely unchanged and varying in the range $0 \leq \rho < 3.5$ (upper panels in Figs. 11–12 correspond to ∼20 days, bottom ones correspond to ∼40 days). Activating the submesoscale (random) component entails dynamical patterns similar to the case of the stationary mesoscale field. Purely rotational submesoscales (EXP2) in Figs. 11–12) induce fuzziness of the tracer boundaries, similar to the effect of diffusion,

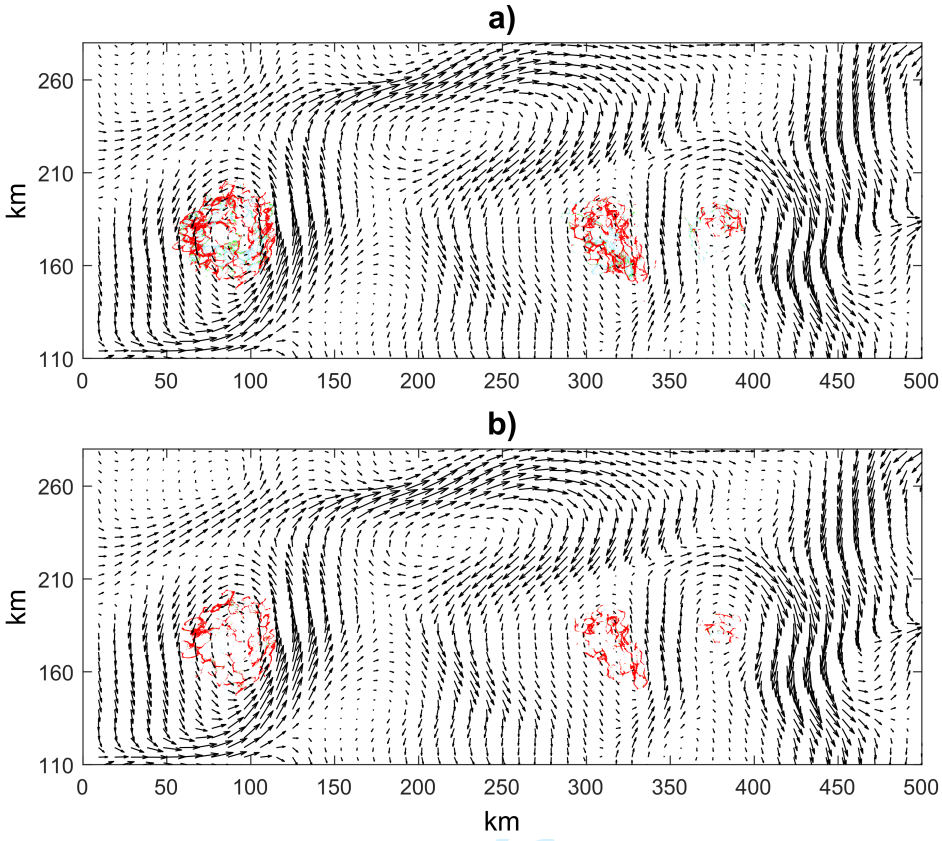

Figure 8. The same as in figure 6, but for EXP3 after: a) 20 days ($\tau = 7.915718$), b) 40 days ($\tau = 15.831436$). Tracer is mostly clustered (high density values in red) within the regions of interest forming patterns of elongated stripes. (Colour online).

whilst the density values remain mostly unchanged ($\rho \leq 4.4$). As expected, no exponential clustering occurs without the divergent flow component.

Purely divergent submesoscales (EXP3) induce partial tracer clustering with relatively large density values for both deployment sites. At $t = 20$ days the values are $\rho \gtrsim 1.5 \times 10^3$ in the cyclonic eddy and $\rho \gtrsim 0.5 \times 10^3$ in the anticyclonic one. At ~ 40 days almost all the tracer is aggregated in patches of density larger than $\rho = 10$; the maximum values attain $\rho \gtrsim 2 \times 10^3$ and 1.5×10^3 for the cyclonic and anticyclonic eddies, respectively. These values are clearly many orders of magnitude smaller than the ones obtained for the steady deterministic velocity case, implying that the flow unsteadiness inhibits clustering. The mixed submesoscale velocity (EXP4) induces similar patterns with partially clustered tracer. The maximum density values ($\rho \sim 200$ for the cyclonic eddy and $\rho \sim 100$ for the anticyclonic one, at both reference times) are again many orders of magnitude smaller than their counterparts in the steady deterministic case, thus, confirming the conclusion.

Now, we again resort to the statistical topography characteristics. Only purely divergent mesoscale component (EXP3) is considered. The statistical topography curves (figure 13) correspond to the deployment sites with the mean patterns shown in figure 2: the cyclonic eddy C, the anticyclone/anticyclone/cyclone tripole AAC, and 2 isolated anticyclones A1 and A2.

Logarithmic-scale clustering area rates can be sorted into 4 distinct regimes (i)–(iv), for all the initial deployment sites. (i) The first one corresponds to weak influence of the deterministic component at earlier times ($\sim 2\tau_p - 4\tau_p$). The clustering mass and area change almost exponentially, similar to the theoretical curves (17), i.e., for $D_p = 1/\tau_p \approx D_0$. (ii) At later

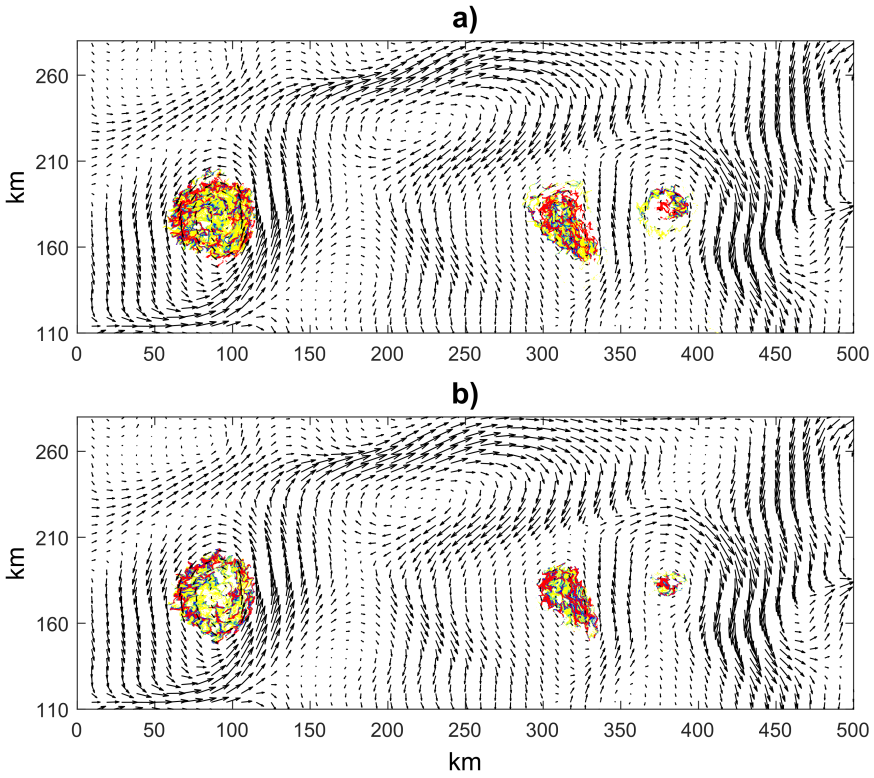

Figure 9. The same as in figure 6, but for EXP4 after: a) 20 days ($\tau = 1.978930$), b) 40 days ($\tau = 3.957860$). Significant part of the tracer is clustered (high density values in red), however the rate of clustering is much slower than in the purely divergent case. (Colour online).

times ($\sim 5 - 10\tau_p$), the clustering rates drastically decrease, so that the tracer density stops increasing. We hypothesise that this behaviour is caused by the fast advection induced by the nonstationary deterministic component. The exact timing, when this regime starts depends one the details of the deterministic field structure. (iii) At intermediate times (from $\sim 6-12\tau_p$ to $\sim 14-22\tau_p$), there is again exponential clustering but at reduced rates, compared to regime (i), where the clustering rates are determined by the diffusion coefficient of the divergent flow component. Compared with the effective diffusion coefficients (figure 13(b)), the exponential clustering occurs at reduced rates in the range $\sim 0.35D_p$ for A1, and $\sim 0.8D_p$ for A2. The clustering rates are, similar to the previous regime and sensitive to the deployment sites. (iv) Further in time, the clustering rates increase again, due to the fact that there is less tracer left in the area of interest (figure 13(a,d)), and the tracer is now largely localised in stagnation zones, where it is less perturbed by the underlying nonstationarity.

The clustering mass behaves differently: at any time its rates are slower than the area shrinkage rates; its initial fast-clustering interval is noticeably shorter (up to $\tau \sim 4 - 5\tau_p$). Further in time, mass accumulation stops, except for case C. Another exponential regime takes place over times from $\tau \sim 6\tau_p$ to $\tau \sim 10\tau_p$, and with significantly reduced rates. After $\tau \sim 10\tau_p$, the clustering mass starts decreasing, nevertheless, large portion of the tracer ($\sim 0.7 - 0.9$ from the initial mass) is already clustered and remains so for long time.

6. Discussion and conclusions

In this paper we quantified floating-tracer clustering phenomena constrained by a nonstationary mesoscale field featuring distinct eddies. This research is motivated by the increasing interest in the transport of floating tracers at the ocean surface.

The flow velocity field governing the tracer evolution is considered to be a combination of a mesoscale (deterministic) component and a submesoscale (random) one. The determin-

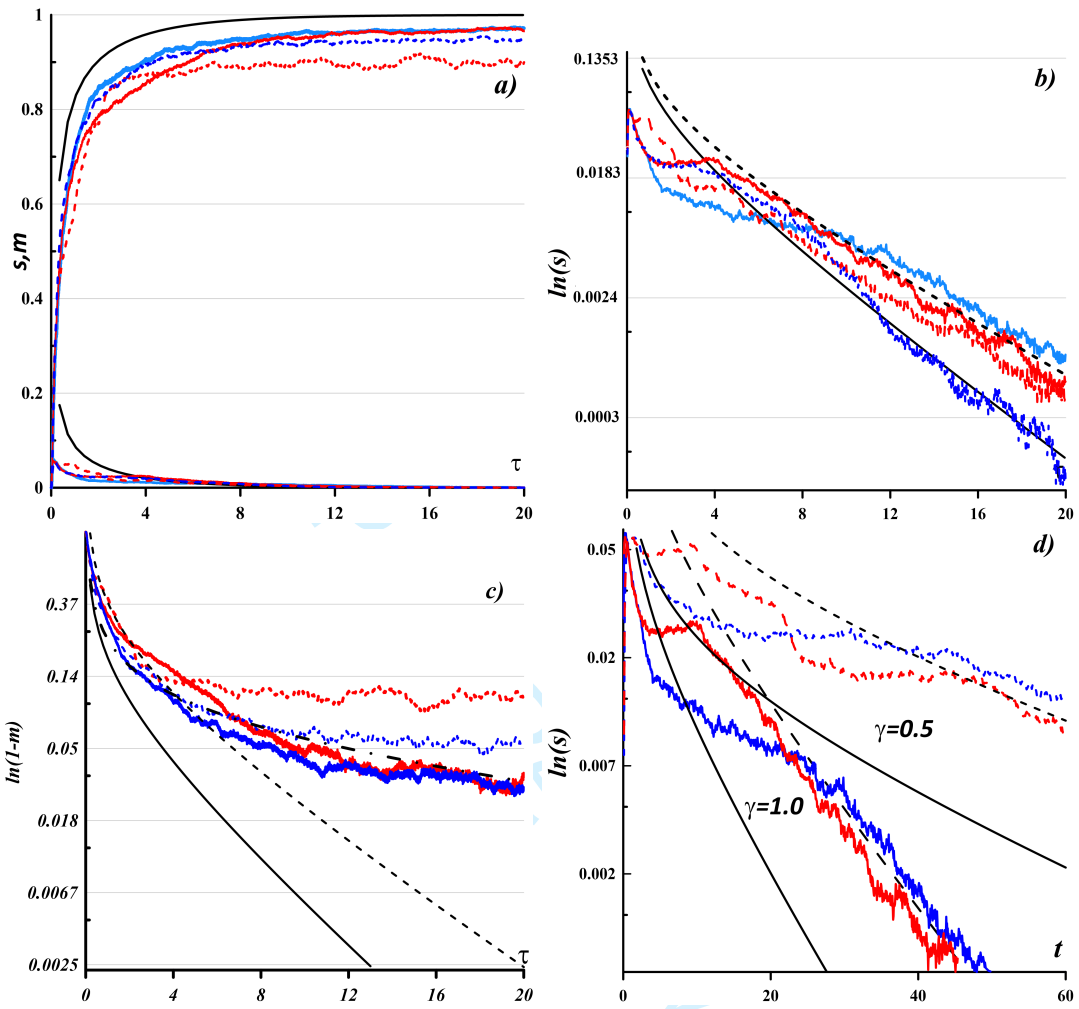

Figure 10. Accumulated clustering mass and area exceeding the threshold $\bar{\rho} = 2$ for EXP3 (solid curves) and EXP4 (dashed curves) velocity cases. The blue curves correspond to the initial deployment region encompassing the cyclonic eddy C, the red ones correspond to the anticyclone/cyclone pair AC; τ is the time scaled by diffusion time (18).
a) Accumulated clustering mass (top curves) and area (bottom curves). The thick black curves show the theoretical limit for the purely divergent velocity field without deterministic component, for $D_p = 1/\tau_p = \gamma^2 D_0$. The dashed black line corresponds to $D_p = 1/\tau_p = 0.75\gamma^2 D_0$. Exponential clustering rates are deduced from the shapes of the curves. b) Accumulated clustering area in the logarithmic scale for the same time scaling as in a). c) Accumulated clustering mass $((m_0 - m(\tau))/m_0)$ normalised by m_0. The time scaling is as in a). The thick black curves show the theoretical limit for the purely divergent velocity field without a deterministic component for $D_p = 1/\tau_p = \gamma^2 D_0$. The dashed black line corresponds to the $D_p = 1/\tau_p = 0.75\gamma^2 D_0$, the dash-dot line corresponds the $D_p = 1/\tau_p = 0.15\gamma^2 D_0$. d) Accumulated clustering area in the logarithmic scale depending on the physical time t (in days). The thick black curves show the theoretical limit (16) for the purely divergent velocity field without a deterministic component for $D_p = \gamma^2 D_0$. The dashed black line corresponds to the $D_p = 0.75\gamma^2 D_0$. (Colour online).

istic component, which is an output of a realistic eddy-resolving circulation model for the Japan/East Sea, features regions of intense mesoscale variability. Then, a kinematic random divergent velocity field is added to account for submesoscale motions. Statistical topography characteristics are used to quantify the ensuing clustering in the combined velocity field.

Comparison of the clustering processes in the steady and unsteady mesoscale velocity fields reveals that at earlier times ($\sim 2\tau_p$, where τ_p is the specific diffusion time of the random velocity, there is ongoing clustering. However, on longer times ($\sim 4 - 7\tau_p$) the steady deterministic velocity still yields the exponential clustering, whereas the unsteady mesoscale velocity significantly inhibits the clustering and eventually caps it. Moreover, at the later times the unsteady mesoscale velocity reverses the clustering, resulting in negative clustering rates (we see this in the regions of energetic fluctuations after $\sim 20\tau_p$). The statistical topography curves, being

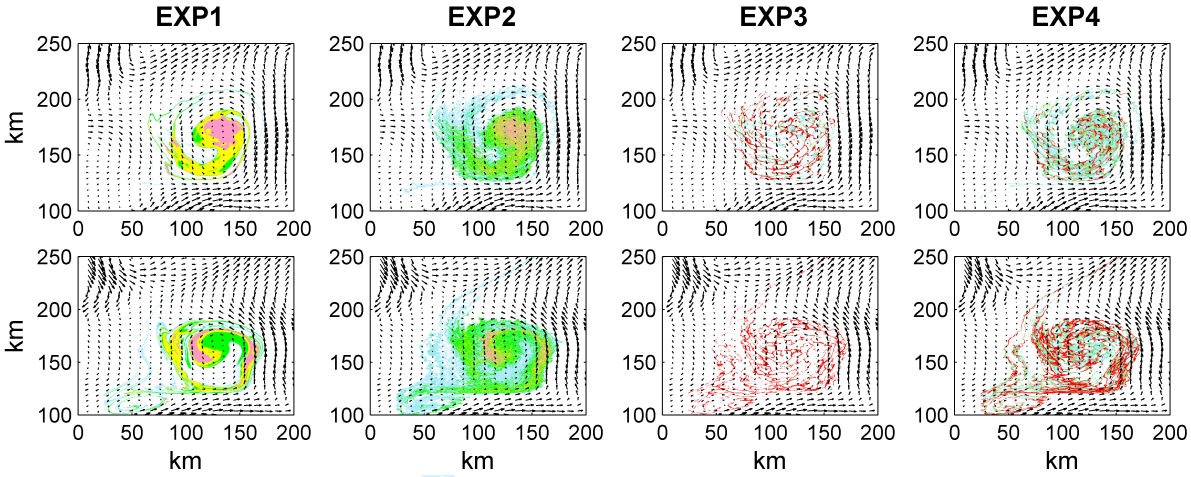

Figure 11. Tracer density evolution (density is colour-coded) for the C (cyclonic eddy) region from figure 2 for the nonstationary deterministic velocity case, otherwise, as in EXP1–EXP4. Upper panel: ∼20 days ($\tau = 1.978930$ at $\gamma = 0.5$ and $\tau = 7.915718$ at $\gamma = 1.0$); bottom panel: ∼40 days ($\tau = 3.957860$ at $\gamma = 0.5$ and $\tau = 15.831436$ at $\gamma = 1.0$). Top row corresponds to ~ 20 days, bottom row corresponds to ~ 40 days. (Colour online).

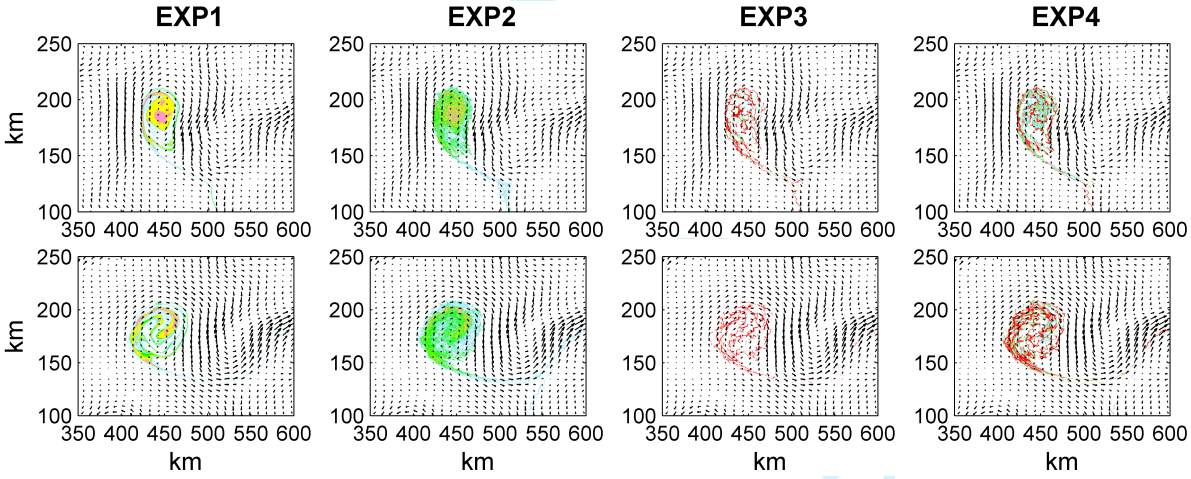

Figure 12. The same as in figure 11, but for the A1 (anticyclonic eddy) region. (Colour online).

integral proxies for clustering, are inconclusive in determining the underlying dynamics that engenders this salient behaviour. The reason for that may be that the mesoscale dynamics is too intense in the regions of interest, and, thus, the tracer is noticeably stirred by chaotic advection. In other words, the characteristic times of clustering are much longer than those of the mesoscale eddies. The intricacy of the interplay between clustering and chaotic advection induced by the underlying mesoscale flow is an interesting issue that can be addressed in more detail by employing simplified vortex models with nonstationary dynamics (e.g., distributed elliptic or ellipsoid vortices (Zhmur *et al.* 2011, Koshel *et al.* 2013, 2015, Koshel and Ryzhov 2016, 2017, Ryzhov 2017).

It is worth mentioning that the full deterministic velocity field governs also processes at faster time scales (7 days), particularly the inertial oscillations, along with meso- and large scale processes. These faster oscillations were filtered out before clustering analyses. However, a few experiments were carried out (not presented) for the full deterministic velocity field and showed very little difference. This is caused by the dominant influence of the mesoscale processes on the clustering dynamics as compared to the inertial oscillations. However, this

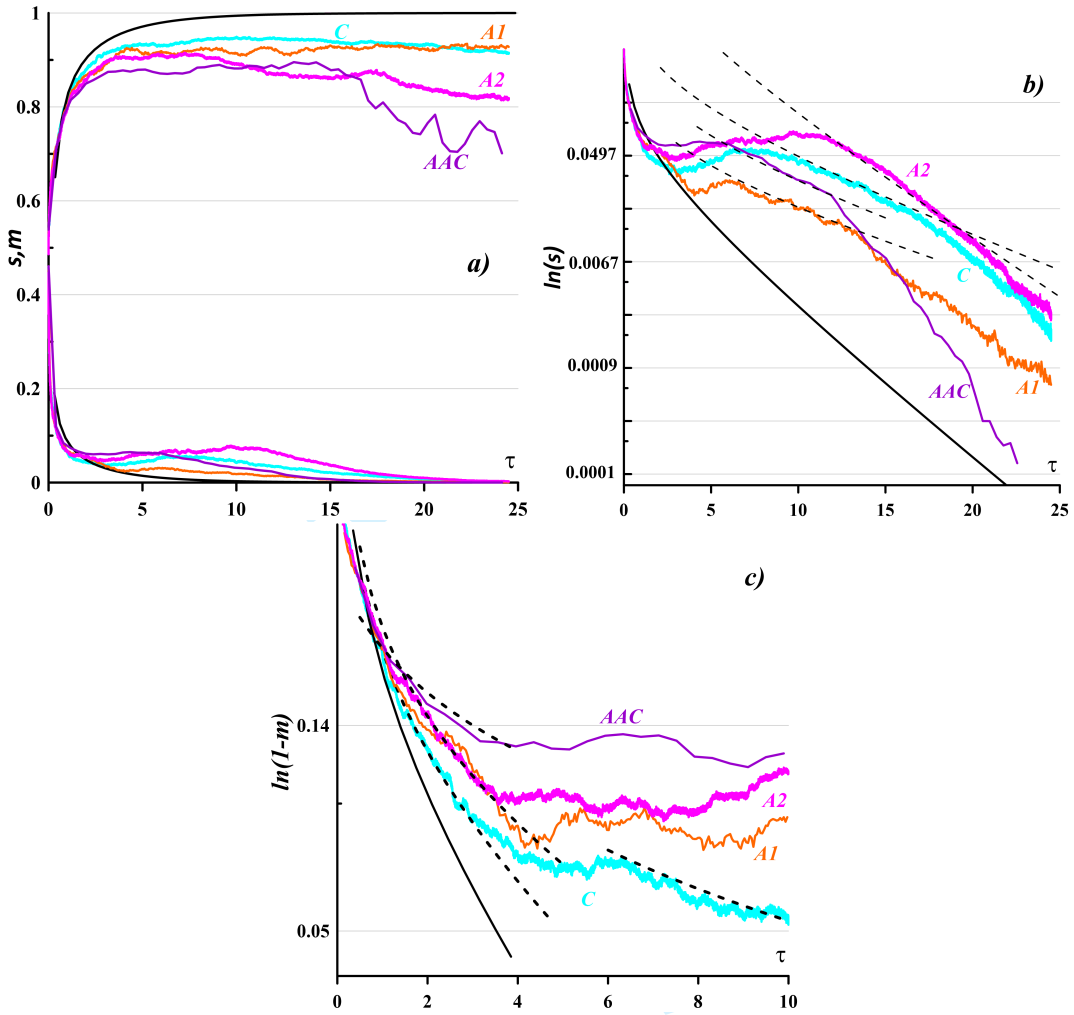

Figure 13. Clustering mass and area for EXP3 when the threshold $\bar{\rho} = 2$. Different colours correspond to the tracer deployment sites: isolated anticyclones A1, A2; cyclone C, and the anticyclone/anticyclone/cyclone tripole AAC; $\tau = t/\tau_p$, and $\tau_p = 2.526$days. a) Mass (top curves) and area (bottom curves). The thick black curve shows the theoretical limit for the purely divergent velocity field without deterministic component (16), (17). The rates of clustering are inhibited by stirring due to the unsteadiness of the deterministic mesoscale component. The AAC dynamical pattern, which favours extremely fast stirring, almost completely inhibits clustering, until the particles are advected out of the domain. b) Only clustering area in the logarithmic scale. The dashed lines show the theoretical limit for the purely divergent velocity field without deterministic component (17) for $D_p = 1/\tau_P$: A1 - $0.35D_0$; AAC - $0.4D_0$; C- $0.45D_0$; A2 – $0.8D_0$. c) Only normalised clustering mass $(m_0 - m(\tau))/m_0$ in the logarithmic scale. The dashed lines show the theoretical limit for the purely divergent velocity field without deterministic component (16) for $D_p = 1/\tau_P \approx$: A1,A2 – $0.35D_0$; AAC - $0.06D_0$; C- $0.57D_0$ and $0.1D_0$. (Colour online).

may be attributed to our specific choice of parameters for the random velocity field, while the clustering theory may also be pertinent to inertial oscillations in the ocean and will be addressed elsewhere.

A detailed study of the clustering sensitivities to parameters γ, σ_U and l (in the vein of Berloff and McWilliams 2003) is needed for extending the approach. This in turn relates to a more pressing problem of establishing relative contributions of mesoscale and submesoscale flows as the main factors for tracer transport in the ocean (McWilliams 2016). Our approach may prove useful in addressing this problem with kinematically modelled submesoscales, as a cheaper alternative to expensive submesoscale-resolving simulations, which are unfeasible for many practical purposes.

Acknowledgements

This study was partially supported by the POI FEB RAS Program "Mathematical simulation and analysis of dynamical processes in the ocean" ($AAAA - A117030110034 - 7$) and by the Russian Foundation for Basic Research projects $19 - 55 - 10001$, $20 - 05 - 00083$. The contribution of KVK in obtaining the analytical estimates was supported by the Russian Scientific Foundation project $19 - 17 - 00006$. PB gratefully acknowledges support from the NERC grants $NE/R011567/1$, $NE/T002220/1$, the Leverhulme grant $RPG - 2019 - 024$, and the Royal Society Exchange Grant $IEC/R2/181033$. The numerical simulation outputs were obtained using the Shared Resource Centre "Far Eastern Computing Resource" IACP FEB RAS (`https://www.cc.dvo.ru`). Data are available `https://www.researchgate.net/publication/340681613_GAFD_dataset`).

References

Abernathey, R. and Haller, G., Transport by Lagrangian vortices in the Eastern Pacific. *J. Phys. Oceanogr.*, 2018, **48**, 667–685.

Bachman, S.D., Fox-Kemper, B. and Pearson, B., A scale-aware subgrid model for quasi-geostrophic turbulence. *J. Geophys. Res.: Oceans*, 2017, **122**, 1529–1554.

Barbosa Aguiar, A.C., Peliz, A. and Carton, X., A census of Meddies in a long-term high-resolution simulation. *Prog. Oceanogr.*, 2013, **116**, 80–94.

Bec, J., Gawedzki, K. and Horvai, P., Multifractal clustering in compressible flows. *Phys. Rev. Lett.*, 2004, **92**, 224501.

Berloff, P.S. and McWilliams, J., Material transport in oceanic gyres. Part III: Randomized stochastic models. *J. Phys. Oceanogr.*, 2003, **33**, 1416–1445.

Berloff, P., Dynamically consistent parameterization of mesoscale eddies. Part III: Deterministic approach. *Ocean Modelling*, 2018, **127**, 1 – 15.

Berta, M., Griffa, A., Özgökmen, T.M. and Poje, A.C., Submesoscale evolution of surface drifter triads in the Gulf of Mexico. *Geophys. Res. Lett.*, 2016, **43**, 11,751–11,759.

Berti, S., Santos, F.A.D., Lacorata, G. and Vulpiani, A., Lagrangian drifter dispersion in the Southwestern Atlantic Ocean. *J. Phys. Oceanogr.*, 2011, **41**, 1659–1672.

Chang, K.I., Zhang, C.I., Park, C., Kang, D.J., Ju, S.J., Lee, S.H. and Wimbush, M., *Oceanography of the East Sea (Japan Sea)*, 2016 (Springer).

Chang, K. and Teague, W., Circulation and currents in the southwestern East/Japan Sea: Overview and review. *Prog. Oceanogr.*, 2004, **61**, 105–156.

Chelton, D.B., Schlax, M.G. and Samelson, R.M., Global observations of nonlinear mesoscale eddies. *Prog. Oceanogr.*, 2011, **91**, 167–216.

Chelton, D.B., Schlax, M.G., Samelson, R.M. and de Szoeke, R.A., Global observations of large oceanic eddies. *Geophys. Res. Lett.*, 2007, **34**, L15606.

Cozar, A., Echevarria, F., Gonzalez-Gordillo, J.I., Irigoien, X., Ubeda, B., Hernandez-Leon, S., Palma, A.T., Navarro, S., de Lomas, J.G., Ruiz, A., de Puelles, M.L.F. and Duarte, C.M., Plastic debris in the open ocean. *Proceedings of the National Academy of Sciences*, 2014, **111**, 10239–10244.

Cressman, J.R. and Goldburg, W.I., Compressible flow: Turbulence at the surface. *J. Stat. Phys.*, 2003, **113**, 875.

Danabasoglu, G., Yeager, S.G., Bailey, D., Behrens, E., Bentsen, M., Bi, D., Biastoch, A., Boning, C., Bozec, A., Canuto, V.M., Cassou, C., Chassignet, E., Coward, A.C., Danilov, S., Diansky, N., Drange, H., Farneti, R., Fernandez, E., Fogli, P.G., Forget, G., Fujii, Y., Griffies, S.M., Gusev, A., Heimbach, P., Howard, A., Jung, T., Kelley, M., Large, W.G., Leboissetier, A., Lu, J., Madec, G., Marsland, S.J., Masina, S., Navarra, A., Nurser, A.J.G., Pirani, A., Melia, D.S.Y., Samuels, B.L., Scheinert, M., Sidorenko, D., Treguier, A.M., Tsujino, H., Uotila, P., Valcke, S., Voldoire, A. and Wangi, Q., North Atlantic simulations in Coordinated Ocean-ice Reference Experiments phase II (CORE-II). Part I: Mean states. *Ocean Model*, 2014, **73**, 76–107.

Eckhardt, B. and Schumacher, J., Turbulence and passive scalar transport in a free-slip surface. *Phys. Rev. E*, 2001, **64**, 016314.

Falkovich, G., Gawedzki, K. and Vergassola, M., Particles and fields in fluid turbulence. *Rev. Mod. Phys.*, 2001, **73**, 913.

Fouxon, I., Distribution of particles and bubbles in turbulence at a small Stokes number. *Phys. Rev. Lett.*, 2012, **108**, 134502.

Gryanik, V.M., Sokolovskiy, M.A. and Verron, J., Dynamics of heton-like vortices. *Regul. Chaotic Dyn.*, 2006, **11**, 383–434.

Gusev, A.V. and Diansky, N.A., Numerical simulation of the World Ocean circulation and its climatic variability

for 1948–2007 using the INMOM. *Izvestiya, Atmospheric and Oceanic Physics*, 2014, **50**, 1–12.
Haza, A.C., Özgökmen, T.M. and Hogan, P., Impact of submesoscales on surface material distribution in a gulf of Mexico mesoscale eddy. *Ocean Modelling*, 2016, **107**, 28 – 47.
Huntley, H.S., Lipphardt Jr., B.L., Jacobs, G. and Kirwan Jr., A.D., Clusters, deformation, and dilation: Diagnostics for material accumulation regions. *J. Geophys. Res.: Oceans*, 2015, **120**, 6622–6636.
Isichenko, M.B., Percolation, statistical topography, and transport in random media. *Rev. Mod. Phys.*, 1992, **64**, 961–1043.
Jacobs, G.A., Huntley, H.S., Kirwan Jr., A.D., Lipphardt Jr., B.L., Campbell, T., Smith, T., Edwards, K. and Bartels, B., Ocean processes underlying surface clustering. *J. Geophys. Res.: Oceans*, 2016, **121**, 180–197.
Jansen, M.F. and Held, I.M., Parameterizing subgrid-scale eddy effects using energetically consistent backscatter. *Ocean Modelling*, 2014, **80**, 36 – 48.
Jansen, M.F., Held, I.M., Adcroft, A. and Hallberg, R., Energy budget-based backscatter in an eddy permitting primitive equation model. *Ocean Modelling*, 2015, **94**, 15 – 26.
Kloeden, P. and Platen, E., *Numerical Solution of Stochastic Differential Equations*, 1992 (Springer, Berlin).
Klyatskin, V.I., Statistical description of the diffusion of a passive tracer in a random velocity field. *Physics-Uspekhi*, 1994, **37**, 501–513.
Klyatskin, V.I., Clustering and diffusion of particles and passive tracer density in random hydrodynamic flows. *Phys. Usp. 46, 667*, 2003, **46**, 667–688.
Klyatskin, V.I., Stochastic structure formation in random media. *Phys. Usp.*, 2016, **59**, 67–95.
Klyatskin, V.I. and Koshel, K.V., The simplest example of the development of a cluster-structured passive tracer field in random flows. *Physics-Uspekhi*, 2000, **170**, 771–778.
Klyatskin, V.I., *Stochastic Equations: Theory and Applications in Acoustics, Hydrodynamics, Magnetohydrodynamics, and Radiophysics*, Vol. 1,2, 2015 (Springer).
Klyatskin, V. and Koshel, K., Impact of diffusion on surface clustering in random hydrodynamic flows. *Phys. Rev. E*, 2017, **95**, 013109.
Klyatskin, V., Woyczynski, W. and Gurarie, D., Diffusing passive tracers in random incompressible velocity flows: Statistical topography aspects. *J. Stat. Phys.*, 1996a, **84**, 797 – 836.
Klyatskin, V., Woyczynski, W. and Gurarie, D., Short-time correlation approximation for diffusing tracers in random velocity fields: a functional approachb; in *Stochastic Modeling in Oceanography*, edited by R. Adler, P. Muller and B. Razovsky, Vol. 39 of *Progress in Probability*, 1996b, pp. 221 – 269.
Koshel, K.V. and Alexandrova, O.V., Some results of a numerical modeling of the diffusion of passive tracers in a random field of velocities. *Izv. Atmos. Ocean. Phys.*, 1999, **35**, 578–588.
Koshel, K.V. and Ryzhov, E.A., Local parametric instability near elliptic points in vortex flows under shear deformation. *Chaos*, 2016, **26**, 083111.
Koshel, K.V. and Ryzhov, E.A., Parametric resonance in the dynamics of an elliptic vortex in a periodically strained environment. *Nonlin. Processes Geophys.*, 2017, **24**, 1–8.
Koshel, K.V., Ryzhov, E.A. and Zhmur, V.V., Diffusion-affected passive scalar transport in an ellipsoidal vortex in a shear flow. *Nonlin. Processes Geophys.*, 2013, **20**, 437–444.
Koshel, K.V., Ryzhov, E.A. and Zhmur, V.V., Effect of the vertical component of diffusion on passive scalar transport in an isolated vortex model. *Phys. Rev. E*, 2015, **92**, 053021.
Koshel, K.V., Ryzhov, E.A. and Carton, X.J., Vortex interactions subjected to deformation flows: A review. *Fluids*, 2019a, **4**.
Koshel, K.V., Stepanov, D.V., Ryzhov, E.A., Berloff, P. and Klyatskin, V.I., Clustering of floating tracers in weakly divergent velocity fields. *Phys. Rev. E*, 2019b, **100**, 063108.
Large, W. and Yeager, S., The global climatology of an interannually varying air–sea flux data set. *J. Clim.*, 2009, **33**, 341–364.
Law, K.L., Moret-Ferguson, S., Maximenko, N.A., Proskurowski, G., Peacock, E.E., Hafner, J. and Reddy, C.M., Plastic accumulation in the North Atlantic subtropical gyre. *Science*, 2010, **329**, 1185–1188.
Locarnini, R., Mishonov, A., Antonov, J.I., Boyer, T., Garcia, H., Baranova, O., Zweng, M., Paver, C., Reagan, J., Johnson, D., Hamilton, M. and Seidov, D., World Ocean Atlas 2013, Volume 1: Temperature. 2013, Technical report.
Marchuk, G.I., Rusakov, A.S., Zalesny, V.B. and Diansky, N.A., Splitting numerical technique with application to the high resolution simulation of the Indian Ocean circulation. *Pure Appl. Geophys.*, 2005, **162**, 1407–1429.
Martinez, E., Maamaatuaiahutapu, K. and Taillandier, V., Floating marine debris surface drift: Convergence and accumulation toward the South Pacific subtropical gyre. *Mar. Pollut. Bull.*, 2009, **58**, 1347 – 1355.
Maximenko, N., Hafner, J. and Niiler, P., Pathways of marine debris derived from trajectories of Lagrangian drifters. *Mar. Pollut. Bull.*, 2012, **65**, 51–62.
McComb, W.D., *The Physics of Fluid Turbulence*, Vol. 25, Oxford Engineering Sci. Ser. 1990 (Oxford: Clarendon Press).
McWilliams, J.C., The emergence of isolated coherent vortices in turbulent flow. *J. Fluid Mech.*, 1984, **146**, 21–43.
McWilliams, J.C., Submesoscale currents in the ocean. *Proc. R. Soc. A*, 2016, **472**, 20160117.
McWilliams, J.C., The Nature and Consequences of Oceanic Eddies. In *Ocean Modeling in an Eddying Regime*, edited by M. Hecht and H. Hasumi, pp. 5–15, 2013 (American Geophysical Union (AGU): Washington, DC).
Ohlmann, J.C., Romero, L., Pallàs-Sanz, E. and Perez-Brunius, P., Anisotropy in coastal ocean relative dispersion observations. *Geophys. Res. Lett.*, 2019, **46**, 879–888.

Okubo, A., *Diffusion and Ecological Problems: Mathematical Models*, Vol. 10, Biomathematics 1980 (Berlin: Springer-Verlag).

Pacanowski, R. and Philander, S., Parameterization of vertical mixing in numerical models of Tropical Oceans. *J. Phys. Oceanogr.*, 1981, **11**, 1443–1451.

Pedlosky, J., *Ocean Circulation Theory*, 1996 (New York: Springer).

Reznik, G.M., Dynamics of localized vortices on the beta plane. *Izv. Atmos. Ocean. Phys.*, 2010, **46**, 784–797.

Reznik, G.M. and Kizner, Z., Singular vortices in regular flows. *Theor. Comput. Fluid Dyn.*, 2010, **24**, 65–75.

Roberts, A.P. and Teubner, M., Transport properties of heterogeneous materials derived from Gaussian random fields: Bounds and simulation. *Phys. Rev. E*, 1995, **51**, 4141.

Ryzhov, E.A., Nonlinear dynamics of an elliptic vortex embedded in an oscillatory shear flow. *Chaos*, 2017, **27**, 113101.

Saichev, A. and Woyczynski, W., Probability distributions of passive tracers in randomly moving media; in *Stochastic Models in Geosystems*, edited by S. Molchanov and W. Woyczynski, Vol. 85 of *IMA Volumes in Mathematics and its Applications*, 1996, pp. 359 – 400.

Samelson, R.M., Lagrangian motion, coherent structures, and lines of persistent material strain. *Annu. Rev. Mar. Sci.*, 2013, **5**, 137–163.

Schroeder, K., Chiggiato, J., Haza, A.C., Griffa, A., Özgökmen, T.M., Zanasca, P., Molcard, A., Borghini, M., Poulain, P.M., Gerin, R., Zambianchi, E., Falco, P. and Trees, C., Targeted Lagrangian sampling of submesoscale dispersion at a coastal frontal zone. *Geophys. Res. Lett.*, 2012, **39**.

Schumacher, J. and Eckhardt, B., Clustering dynamics of Lagrangian tracers in free-surface flows. *Phys. Rev. E*, 2002, **66**, 017303.

Shevchenko, I. and Berloff, P., Eddy backscatter and counter-rotating gyre anomalies of midlatitude ocean dynamics. *Fluids*, 2016, **1**.

Sokolovskiy, M.A. and Verron, J., *Dynamics of Vortex Structures in a Stratified Rotating Fluid*, 2014 (Springer, Switzerland).

Stepanov, D.V., Estimating the baroclinic Rossby radius of deformation in the Sea of Okhotsk. *Russian Meteorology and Hydrology*, 2017, **42**, 601–606.

Stepanov, D.V., Mesoscale eddies and baroclinic instability over the eastern Sakhalin shelf of the Sea of Okhotsk: a model-based analysis. *Ocean Dynamics*, 2018, **68**, 1353 – 1370.

Stepanov, D.V., Diansky, N.A. and Fomin, V.V., Eddy energy sources and mesoscale eddies in the Sea of Okhotsk. *Ocean Dynamics*, 2018, **68**, 825 – 845.

Stepanov, D.V., Ryzhov, E.A., Zagumennov, A.A., Berloff, P. and Koshel, K.V., Clustering of floating tracer due to mesoscale vortex and submesoscale fields. *Geophys. Res. Lett.*, 2020.

Tsujino, H., Urakawa, S., Nakano, H., Small, R.J., Kim, W.M., Yeager, S.G., Danabasoglu, G., Suzuki, T., Bamber, J.L., Bentsen, M., Böning, C.W., Bozec, A., Chassignet, E.P., Curchitser, E., Boeira Dias, F., Durack, P.J., Griffies, S.M., Harada, Y., Ilicak, M., Josey, S.A., Kobayashi, C., Kobayashi, S., Komuro, Y., Large, W.G., Le Sommer, J., Marsland, S.J., Masina, S., Scheinert, M., Tomita, H., Valdivieso, M. and Yamazaki, D., JRA-55 based surface dataset for driving ocean–sea-ice models (JRA55-do). *Ocean Model*, 2018, **130**, 79–139.

Väli, G., Zhurbas, V.M., Laanemets, J. and Lips, U., Clustering of floating particles due to submesoscale dynamics: a simulation study for the Gulf of Finland, Baltic Sea. *Fundamentalnaya i Prikladnaya Gidrofizika*, 2018, **11**, 21–35.

Vallis, G.K., *Atmospheric and Oceanic Fluid Dynamics*, 2017 (Cambridge: Cambridge University Press).

Yakovlev, N.G., Reproduction of the large-scale state of water and sea ice in the Arctic Ocean in 1948–2002: Part I. Numerical model. *Izvestiya, Atmospheric and Oceanic Physics*, 2009, **45**, 357–371.

Zalesny, V.B., Agoshkov, V.I., Aps, R., Shutyaev, V., Zayachkovskiy, A., Goerlandt, F. and Kujala, P., Numerical modeling of marine circulation, pollution assessment and optimal ship routes. *Journal of Marine Science and Engineering*, 2017, **5**, 27.

Zhmur, V.V., Ryzhov, E.A. and Koshel, K.V., Ellipsoidal vortex in a nonuniform flow: Dynamics and chaotic advections. *J. Mar. Res.*, 2011, **69**, 435–461.

Zhong, Y. and Bracco, A., Submesoscale impacts on horizontal and vertical transport in the Gulf of Mexico. *J. Geophys. Res.: Oceans*, 2013, **118**, 5651–5668.

Zirbel, C.L. and Cinlar, E., Mass Transport by Brownian Flows; in *Stochastic Models in Geosystems*, edited by S.A. Molchanov and W.A. Woyczynski, IMA Volumes in Mathematics and its Applications, 1997, p. 459.

Zweng, M., Reagan, J., Antonov, J., Locarnini, R., Mishonov, A., Boyer, T., Garcia, H., Baranova, O., Johnson, D., Seidov, D. and Biddle, M., World Ocean Atlas 2013, Volume 2: Salinity. 2013, Technical report.